Interfacial failure in adhesive joints: Experiments and predictions

Luis Ernesto Mendoza Navarro, **Alberto Díaz Díaz**, Rubén Castañeda-Balderas, Stéphane Hunkeler, Romuald Noret.

Abstract

The aim of this paper is the development of a method to predict interfacial failure in adhesive joints. The main originality of the paper resides on the application of a twofold criterion involving stress and energy conditions simultaneously to predict adhesive failure onset in different geometries of adhesive joints subjected to diverse loadings. Butt joints and double lap joints made of linear elastic materials are tested in torsion and tension. The failure onset predictions are based on finite element calculations and a twofold criterion which considers a novel stress condition. These predictions are accurate and prove the validity of the method to predict adhesive failure for different adhesive joint configurations and loadings.

1. Introduction

The use of adhesives has increased considerably in the last decades owing to their advantages against other assembly techniques. The design of adhesively bonded structures requires theoretical tools to predict critical loads and ensure the reliability of the structure. The failure scenarios are: cohesive failure (cracking of the adhesive layer) [1–3], adherent failure [4,5], adhesive failure [3,6,7] (failure of the interface between the adherent and the adhesive) or a combination of these three cases [8]. In a rigorous and detailed analysis, one failure criterion is required for each one of these failure modes. In most of the failure predictions published before,

cohesive and adhesive failures are not distinguished [9]. This is due to the difficulty of calculating interfacial stresses and handling stress singularities. Also, it is widely assumed that in a good design of an adhesive joint, failures occur only within the adhesive layer [9].

In few publications, a criterion of adhesive failure in adhesive joints is proposed. The adhesive failure criteria gathered from literature may be classified by the way interfacial stresses, stress intensity factors or strain energy release rates are applied in the criteria. Crocombe et al. proposed a criterion involving the peel stresses at a characteristic distance from the edge in order to avoid stress singularities [10]. This criterion was based on mechanical tests on adhesive joint specimens that subjected the interfaces to different ratios of normal/shear stresses at the center of the interfaces (far from the edge effect zones). Qian and Akisanya [11] used stress intensity factors to predict the onset of mode I adhesive failure in scarf joints with three different scarf angle values. Kim et al. [12] performed tests on composite single lap bonded joints with different adhesives in order to propose a quadratic stress criterion involving the averages of the interfacial stresses over a characteristic distance from the edge as proposed by Brewer and Lagace [13] for the prediction of free edge delamination in composite laminates. Mendoza-Navarro et al.[14] used a peel stress criterion to forecast failure in T-joints by making use of a layerwise model which provides finite values of the interfacial stresses even at the edges. Another approach consists on adopting a cohesive zone modeling to simulate the progressive damage initiation and propagation. In [15], a cohesive zone model for the interfaces was applied to predict the load-displacement curves and

2

strength of single lap joints. Accurate predictions were obtained. It is worth mentioning that cohesive zone models have been applied by Crocombe and his coworkers to also predict cohesive failure for various types of adhesive joints under several loading and environmental conditions [16–19].

Once the parameters involved in the failure criterion have been identified by means of a test (for instance, a tensile test on a double lap joint), it is natural to try to predict failure onset in other structures (butt joints subjected to torsion, for example) by means of the same failure criterion. Nevertheless, the predictions in other structures are usually not correct in spite of using the same materials [20]. This may be due to manufacturing defects [21], a high experimental scattering, a bad modeling of the behavior of the adhesive (usually a linear elastic behavior is assumed but the behavior is generally non-linear [7]), a weak accuracy of the method applied to calculate stresses [10], a wrong selection of failure criteria and the inability of the predictive method to distinguish adhesive failure from cohesive failure [9]. In answer to the necessity of adhesive failure criteria, in this work, the authors propose experiments with adhesive double lap and butt joints whose failure is initiated by an interfacial failure and prove that a twofold criterion involving simultaneously stress and energy conditions [22,23] is an efficient tool to predict adhesive failure onset. A stress condition, more appropriate than a quadratic stress criterion is proposed in this paper. In the proposed tests, failure modes are very varied: pure mode III and mixed-modes I–II and I–II–III. The substrates used are of low alloy steel and instead of a commercial adhesive a polyester resin that has a quasi linear elastic behavior prior to failure is applied.

The article is structured in four parts. Firstly, materials, specimen types, samples preparation and devices used are described. Then, the results obtained in the mechanical tests are presented. In the third part, a stress analysis of the tests is performed by means of the finite element COMSOL Multiphysics 3.3 software. Finally, the twofold criterion of adhesive failure is determined in order to predict failure for every specimen tested in this paper.

2. Materials and experimental methods

In this part, we describe the materials and methods used to make the specimens and carrying out the tests.

2.1. Specimens for adhesive and substrate characterization

The polyester resin used as adhesive was made by adding a cobalt naphtate catalyst to the base resin with the ratio recommended by the supplier. The adhesive cures after 24 h at an average room temperature of 25 1C. In order to characterize the adhesive mechanical behavior and to evaluate the effect of the hydrostatic stress, three cylindrical specimens were made with a diameter of 12.5 mm to perform compression tests, and five bone-shaped specimens for the tension tests. In these last specimens, the thickness was 2.96 mm and the width was 12.6 mm. The steel in the substrates was characterized by means of three tension tests. These tests were performed with a strain rate of 0.1%/min. All the specimens were instrumented with strain gages for an accurate measurement of strains.

2.2. Adhesive joint tests

In this work, three different types of tests were carried out to submit the interfaces to different normal stress–shear stress ratios. The tests are shown in Fig.

1 and are named as follows:

- Type A: ''Torsion–tension'' tests with butt joint specimens,

- Type B: Tension tests with double lap joints,

- Type C: Peeling tests with double lap joints.

In Fig. 1, the specimen dimensions are specified. The adhesive thickness in all the samples was constant and equal to 0.5 mm. For the overlap length l in type B and C specimens, three values were used: 10 mm, 15 mm, and 20 mm. It is worth telling that for type B specimens, only the overlap length varied in one joint end with the abovementioned values, the overlap length in the other end remained the same, equal to 30 mm.

Type A specimens consist of two coaxial steel cylindrical pieces. For every pair of coaxial metallic pieces, half an urethane slip coupling was inserted in the upper end of the lower piece and the resin was poured into the cavity formed by the upper half of the coupling (see Fig. 2). Afterwards, the upper metallic piece was slipped into the coupling leaving the desired adhesive thickness.
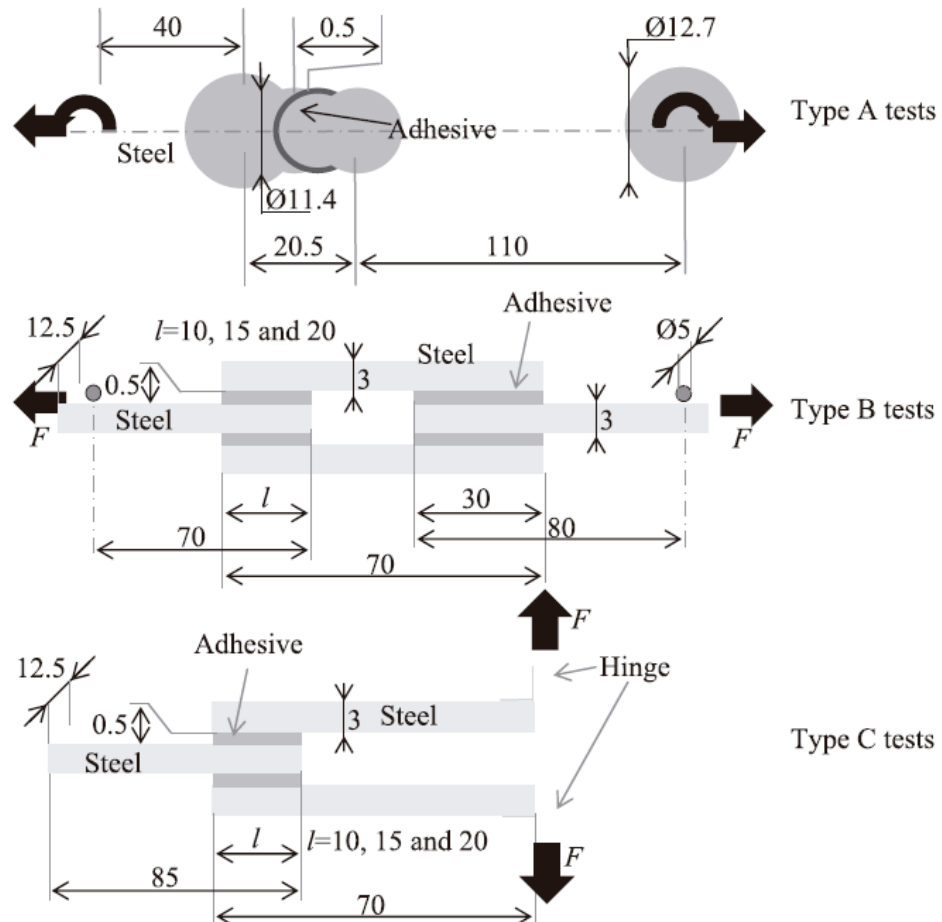
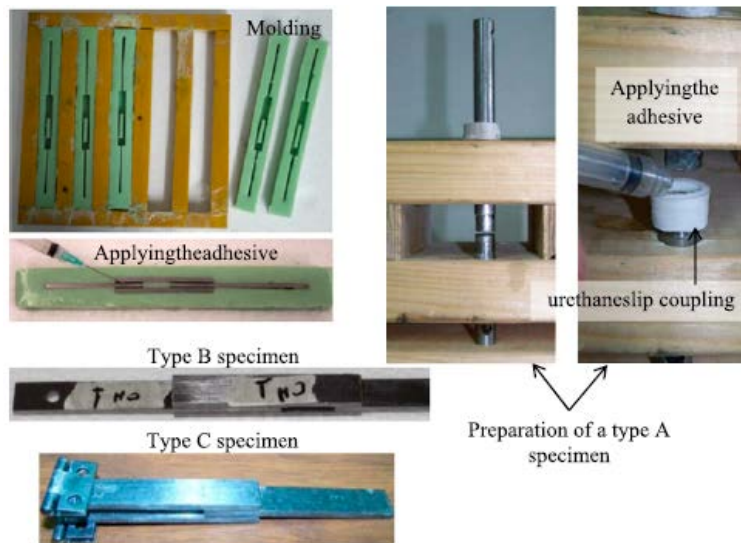Fig. 1. Adhesive joint specimens and dimensions in mm.

Fig. 2. Preparation of adhesive joint specimens.

The correct adhesive thickness was assured by means of stops in the specimen ends. For the construction of specimens B and C, urethane molds were made (see Fig. 2), thanks to machined and calibrated standards. The surfaces of the substrates of all the three types of specimens were grinded for them to have a flat surface and the same roughness in all the tests (the maximum roughness

depth was Rmax¼2 mm). In every case, the surfaces were cleaned with acetone and left drying to apply the adhesive subsequently.

For type A specimens, the device shown in Fig. 3 was used in order to apply simultaneously tensile and torsional loads. The torsional load is applied by means of a lever arm whereas the tensile force is applied by means of a pulley mounted on ball bearing devices. The tensile load F is first applied and then the torque T is increased at a rate of approximately 1 Nm/min: this is done by putting weights in the pan attached to the lever arm. Each weight corresponds approximately to a 0.02 Nm torque. For validation purposes, two pure tension tests were carried out in a universal testing machine and the maximum loads (1.279 and 1.150 kN) were compared with those obtained in two pure tension tests performed in the torsion–tension device (1.130 and 1.083 kN). The results were practically the same.

The tests of type B and C specimens were carried out in a universal testing machine and the displacement rate was 0.1 mm/min. The load in type B specimens was transmitted with pins so as to prevent transmission of parasite moments.

3. Experimental results

3.1. Results for adhesive and steel

In Fig. 4, the axial stress s and the transverse strain et are plotted against the

axial strain eax for a representative polyester specimen subjected to tension and compression. In compression, the adhesive has an elastoplastic behavior that makes possible to reach higher strains than in tension. This usually happens with thermoset polymers (such as structural adhesives) with yield function and failure criterion depending on hydrostatic stress [24]. The stress–strain curves obtained with the five tensile tests are shown in Fig. 5; a small dispersion of results and a quasi linear elastic behavior can be observed in this figure. The averages (standard deviation) for Young's modulus E, maximum stress smax and Poisson's ratio n obtained in the 5 tension and 3 compression tests are listed in Table 1. The maximum stress in tension reported herein should be considered with caution because size
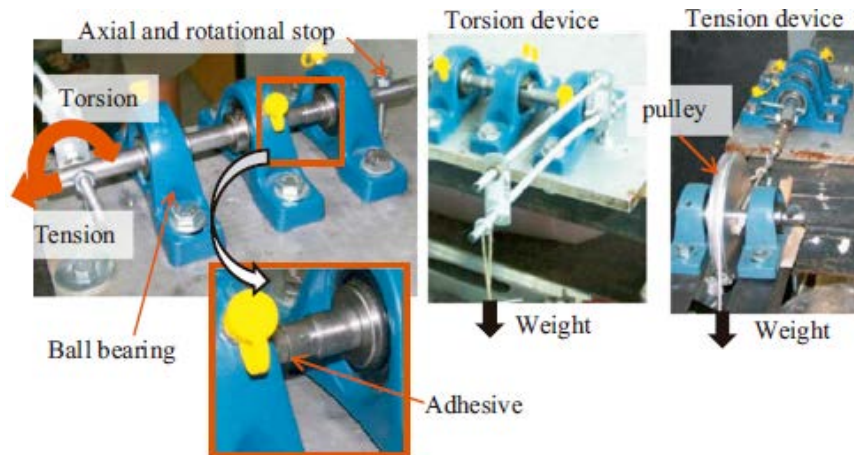

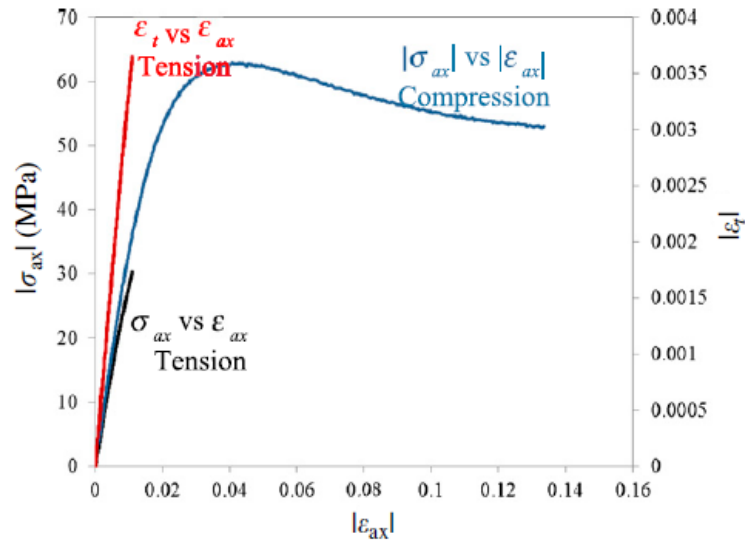Fig. 3. Experimental device used to perform type A tests.

Fig. 4. Axial stress s_{ax} and transverse strain e_t vs. axial strain e_{ax} for the adhesive subjected to tension and compression.
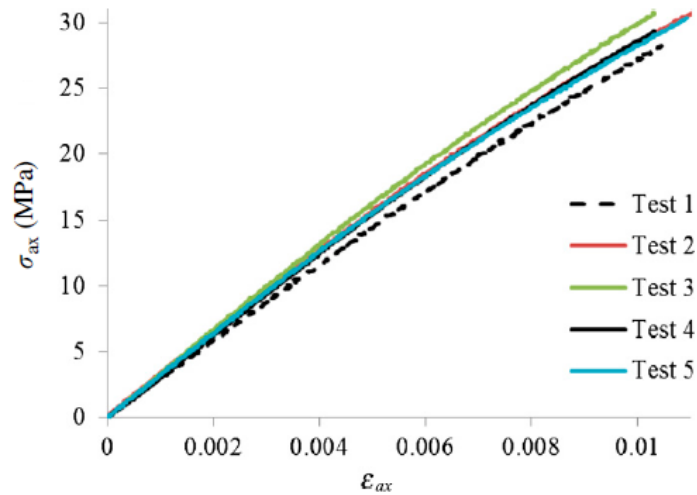

Fig. 5. Axial stress s_{ax} vs. axial strain e_{ax} for the 5 adhesive specimens tested in tension.

Table 1
Averages (standard deviations) of the mechanical properties of the adhesive measured in tension and compression.

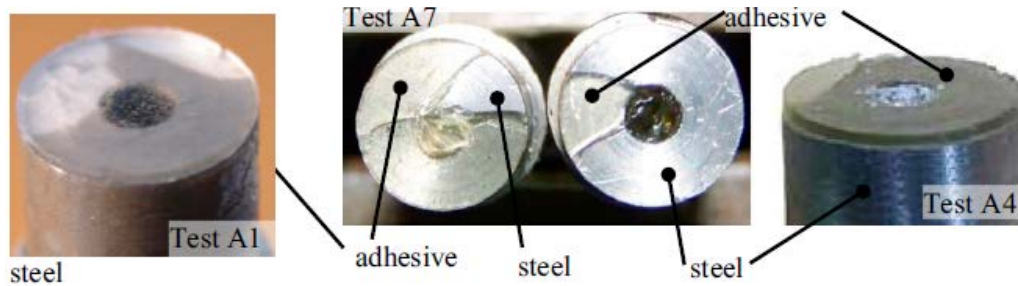|	E (GPa)	v	σ_{max} (MPa)
Tension	3.13 (0.17)	0.35 (0.02)	29.9 (1.1)
Compression	2.90 (0.26)	0.38 (0.02)	66.7 (3.7)

Fig. 6. Typical failures for tests A.

effects may occur and for smaller bulk adhesive specimens the maximum stress may be greater than 29.9 MPa.

For the steel considered in the substrates of the adhesive joints, the averages (standard deviations) for Young's modulus E,

maximum stress smax and Poisson's ratio n obtained in the 3 tension tests are 181 GPa (3 GPa), 210 MPa (9 MPa) and 0.33 (0.03), respectively.

3.2. Type A tests results

For this type of tests, due to the simplicity of the device used, no force vs. displacement graphs were obtained. Only critical combination values of axial force and torque were obtained. Pure tension (test A1), pure torsion (test A7) and combined tension–torsion tests (tests A2–A6) were performed with two repetitions for each test. All the tests carried out had a spontaneous catastrophic failure with an abrupt noise. In every test, an adhesive failure was observed; three pictures displaying typical interfacial failures are shown in Fig. 6. An EDAX analysis was performed to a sample of a failed specimen which seemed to have no adhesive. No cobalt trace was found (cobalt naphtate is the catalyst for the base resin) and this proves that failure was interfacial. The values of force and torque at failure are

provided in Table 2. An important scattering is obtained particularly for tests A2–A6. This may be due to the intrinsic dispersion of the adhesive–substrate interface and to manufacturing defects such as uncontrolled adhesive spew fillets at the edges which affect considerably the large stress concentrations close to the interface. Adams et al. [25] showed how adhesive spew fillets may affect the strength of a butt joint. In general, a decrease of the applied axial load implies an increase of the allowable torque. Addition-ally, in Table 2, the values of the apparent tensile stress (axial force divided by area) and maximum shear stress due to torsion are listed. This shear stress is obtained by the classical torsion formula:

$$\tau = \frac{T}{J}R$$

Where T, J, R stand for the torque, the polar moment of inertia and the radius of the specimen, respectively.

3.3. Type B tests results

For the double lap joint specimens (type B specimens), five tests were carried out for each considered overlap length. In Fig. 7(a–c), the graphs of force vs. displacement in type B tests with the 10 mm, 15 mm and 20 mm overlap length specimens are shown, respectively. The displacement value corresponds to the crosshead displacement provided by the universal testing machine. Therefore, the displacement may not be the same as the elongation of the specimens. The apparent initial non-linear behavior is due to gap adjustments. In Fig. 7(d), the force vs. displacement curve of a particular specimen of each family is shown. This particular specimen was selected by its proximity of

Table 2
Measured loads and stresses at failure for tests A.

Test	Axial force (kN)	Torque (Nm)	Tensile stress (MPa)	Shear stress (MPa)
A1	1.083–1.13	0	10.61–11.07	0
A2	0.773	2.928–3.127	7.57	10.07–10.75
A3	0.650	2.438–3.351	6.37	8.38–11.52
A4	0.523	3.040–3.443	5.12	10.45–11.84
A5	0.434	3.701–4.251	4.25	12.72–14.61
A6	0.193	3.421–4.260	1.89	11.76–14.64
A7	0	4.745–4.824	0	16.31–16.58

Its strength to the average strength of each family. In general, the rigidity and strength increase as the overlap length increases. The failure was catastrophic and occurred spontaneously with an abrupt noise. As shown in Fig. 7 and in spite of the careful preparation of specimens, an important scattering of the strength for each adhesive length is observed. This scattering may be due to manufacturing defects near the intersection of the interfaces with the edges and/or to misalignments of the ends of the specimens which may cause parasite bending moments. The averages of the force values at the failure moment are given in Table 3. The failure scenario was very complex and variable even between specimens having the same overlap length. Adhesive failures jumping from one interface to another occurred and sometimes the interfaces with longer adhesive failed as well. Despite this variability, a constant in all the tests was the failure of interface 2 or 3 indicated in Fig. 8. In this figure, a picture showing the failure of a specimen with a 10 mm overlap length is shown.

3.4. Type C tests results

For each overlap length, three repetitions were performed. In Fig. 9, the graphs of force vs. displacement in type C tests are shown. An important scattering

of strength results can be observed. Once again, this scattering may be due to manufacturing defects. Generally, the rigidity and strength increase as the overlap length increases. This may be due to the change of the moment arm from one test to another. Adhesive failures occurred spontaneously at interfaces 1 or 4 and in some cases the failure jumped to interfaces 2 and 3 as shown in Fig. 10.In Table 3, the averages of the forces leading to failure for every specimen are shown. These forces are by far lower than those obtained for tests B.

4. Stress analysis

Since the adhesive behavior is sensitive to the hydrostatic stress, a Drucker-Prager type elastoplastic model with isotropic hardening was fitted to the experimental curves obtained in Fig. 4 (for more details, see Appendix A). This model was implemented
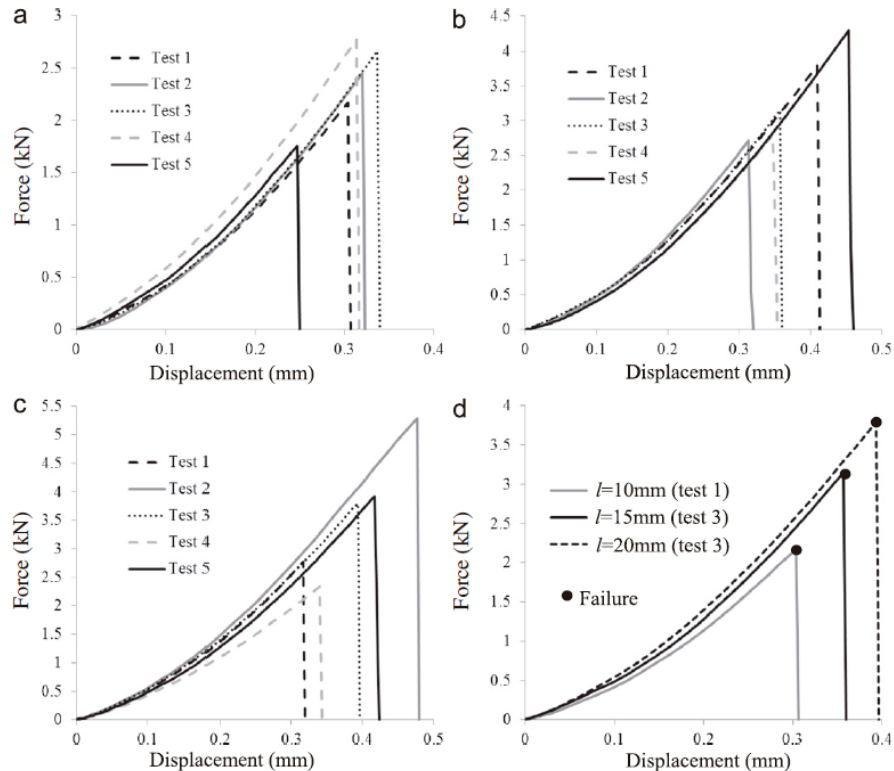

Fig. 7. Force vs. displacement curves for tests B (l=10 mm) (a), l=15 mm (b), l=20 mm (c) and a curve of each overlap length (d).

Table 3
Failure loads for tests B and C.

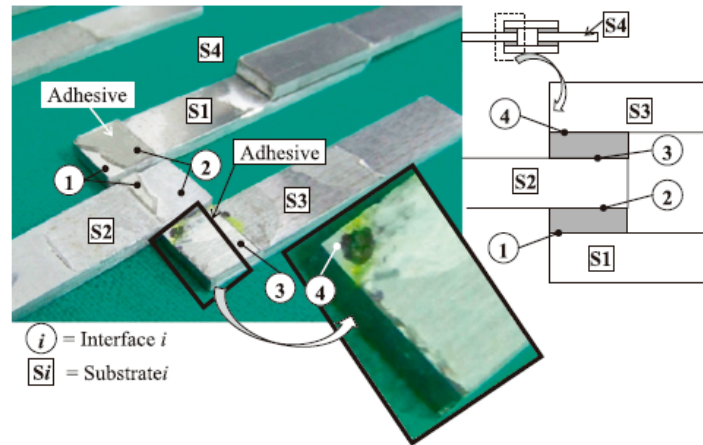| Overlap length (mm)	Failure load-tests B (N)	Failure load-tests C (N)
10	2374^{+406}_{-613}	$45.1^{+5.3}_{-8.3}$
15	3374^{+948}_{-626}	$48.7^{+3.2}_{-6.4}$
20	3632^{+1659}_{-1298}	$51.6^{+9.5}_{-5.6}$

Fig. 8. Failure in a type B specimen ($l=10$ mm).

in COMSOL Multiphysics 3.3 software and a structural analysis was performed for each adhesive joint considered in this paper and subjected to the failure loads that are provided in Tables 2 and 3. Stress singularities existatthe intersection between the interfaces and the free edges and for this reason a finer mesh density was used around these stress singularity points. Triangular elements were selected for the analysis and the smallest element size was 2 mm (the maximum roughness depth measured on the substrates was Rmax¼2 mm). The use of an element size smaller than the roughness of the substrate surface has no sense since this roughness is not taken into account in the modeling. Far enough from the stress singularity points, at a distance greater than 3 ☐ Rmax, the stress results are practically the same as those obtained with a linear elastic assumption. For this reason, the stress analysis shown in this paper is based on a linear elastic

assumption and this makes possible to use the theory of "linear elastic fracture mechanics". Moreover, small strains and displacements are assumed. It is worth mentioning that the numerical results shown in this paper do not depend on the meshing refinement except for the interfacial stresses in the vicinity of stress singularity points. From this point forward, all the calculations are linear elastic.

4.1. Tests A

In order to calculate stresses in cylindrical butt joints subjected to tension and torsion, we adopt a cylindrical coordinate system (r,y,z). The boundary conditions are

- $U_z=U_\theta=\sigma_{rz}=0$ at the bottom boundary,

- $U_z=D$, $U_\theta=r\varphi$, and $\sigma_{rz}=0$ at the top boundary,

- $U_r=\sigma_{r\theta}=\sigma_{rz}=0$ at the axis of symmetry placed on the z-axis,

- $\sigma_{rr}=\sigma_{r\theta}=\sigma_{rz}=0$ at the vertical stress free boundary,
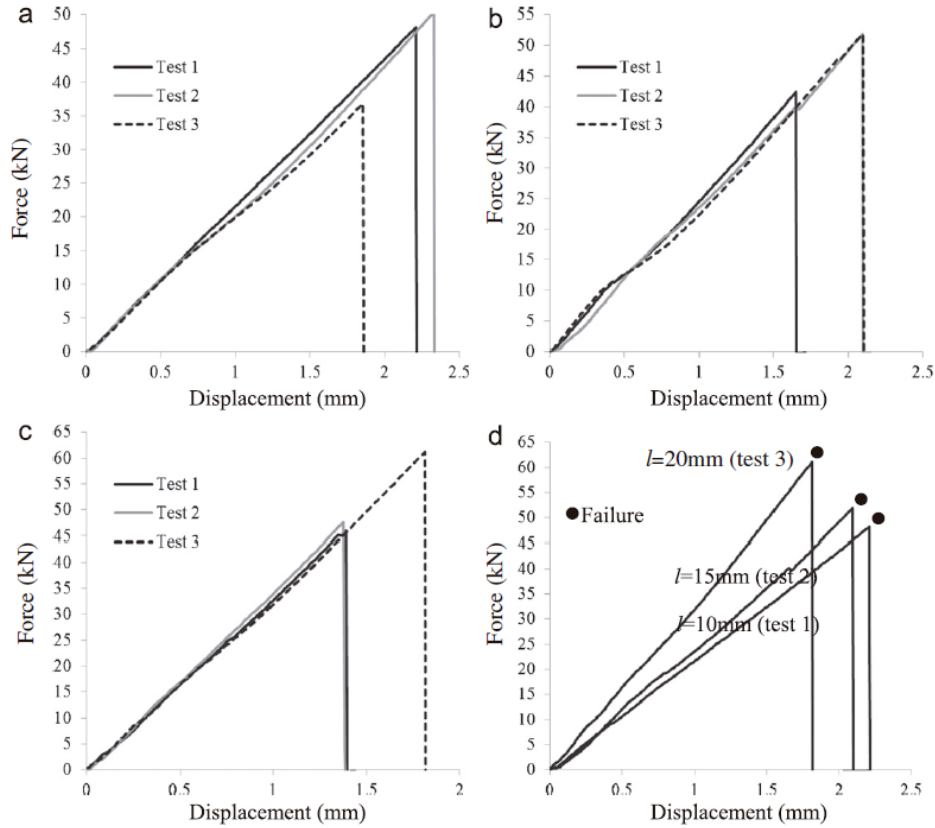
Fig. 9. Force vs. displacement curves for tests C (l=10 mm) (a), l=15 mm (b), l=20 mm (c) and a curve of each overlap length (d).
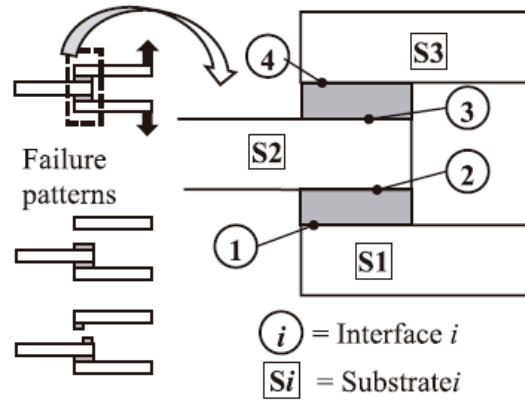

Fig. 10. Failure patterns for tests C.

Where U is the displacement vector, r is the stress tensor, D is the imposed elongation and j is the imposed torsional angle.

A resolution of the mechanical equations in an (r,z) plane is proposed

because displacements, strains and stresses do not depend on the angular coordinate (see Fig. 11). Since the pre-defined axisymmetric equations in COMSOL are not appropriate to this problem (displacements Uy and stresses syz are non-zero), the equations were programmed and solved in the PDE module of COMSOL. Owing to this simplification of the 3D problem, an important saving in computing time and memory required is achieved. In Fig. 11, the meshing used in COMSOL is shown.
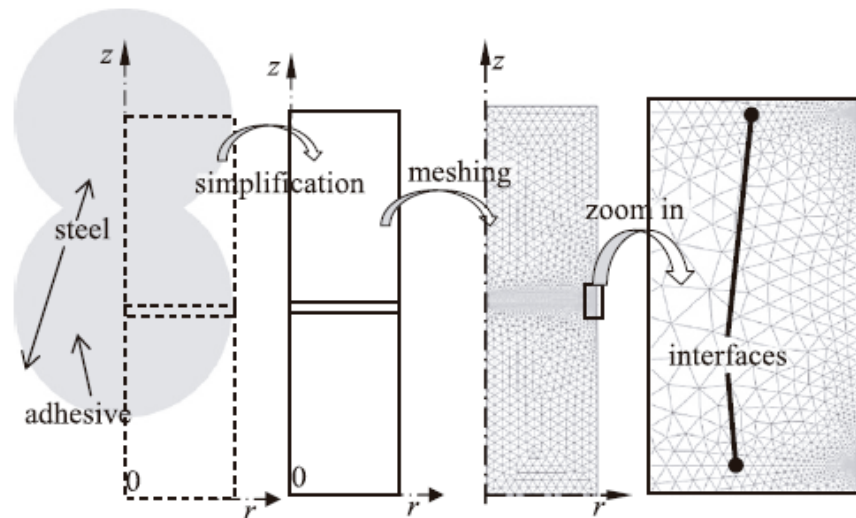

Fig. 11. Modeling and meshing of type A specimens.

The stress state is a result of a superposition of the stresses obtained from the torsion problem and those from the tension problem. In Fig. 12, the plots of the interfacial szz normal and srz shear stresses against the radial position at one interface are shown for the case of a 1 kN axial load. An important edge effect is observed. In this loading case, results at the edge do not converge with mesh refinement due to a stress singularity located at the intersection between the interface and the free edge.

In Fig. 12, the syz shear stress is plotted against the distance from the edge

for the case of a 1 Nm torsional load. It is worth mentioning that for this torsion case no singularities appear and the calculations of stresses converge [25]. The shear stresses may be obtained by the classical torsion formula

$$\sigma_{\theta z} = \frac{T}{J}r$$

Where T, J, r stand for the torque, the polar moment of inertia and the radial position, respectively. Type A tests exhibit then mode III, mixed-mode I–II and mixed-mode I–II–III failures.

4.2. Tests B and C

For type B and C specimens, a plane strain state was considered. In Fig. 13, the meshing example of type B and C specimens is shown with an overlap length of 10 mm. Let us consider this overlap
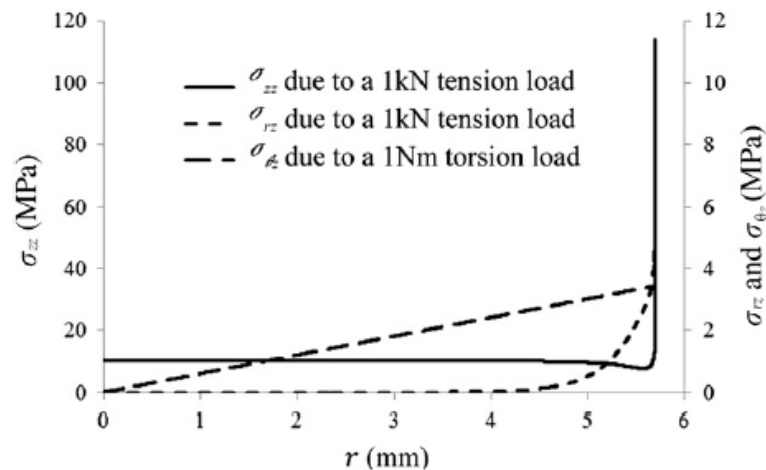

Fig. 12. Interfacial normal and shear stresses (test A).

length for the results analyzed in this paragraph. In Fig. 14, shear and normal stresses at the upper and lower interfaces (shown in Fig. 13) are displayed for the type B specimen subjected to a 2.37 kN load. Higher interfacial stresses appear near the bottom left stress singularity point for specimen B. In Fig. 15, shear and

normal stresses are plotted along the upper and lower interfaces of speci-men C subjected to a 45.1 N load. Higher interfacial stresses appear near the stress singularity point at the right edge of the upper interface of specimen C. It is for this reason, from a stress point of view, that these points (or their symmetric ones) with a higher stress concentration were connected to a crack in the experiments with specimens B and C shown in Section 2. With the plane strain assumption the shear stresses syz are zero, this is valid far enough from the stress free boundaries to which the z-direction is normal. If failure starts in this region, Figs. 14 and 15 predict a mixed mode I–II failure. If failure occurs near the aforementioned stress free boundaries, a mixed mode I–II–III failure occurs because the shear stresses syz are non-zero due to the edge effects.

5. Adhesive failure criterion

5.1. Selection of a failure criterion

In [22], Leguillon proposed an original approach to predict crack nucleation by means of energy and stress conditions. For failure onset (crack nucleation), the energy condition must not involve differential strain energy release rate because its calculation imply a progressive growth of the crack area and if an infinitesimal crack is considered the strain energy release rate tends to zero. Let us consider a static elastic structure without any
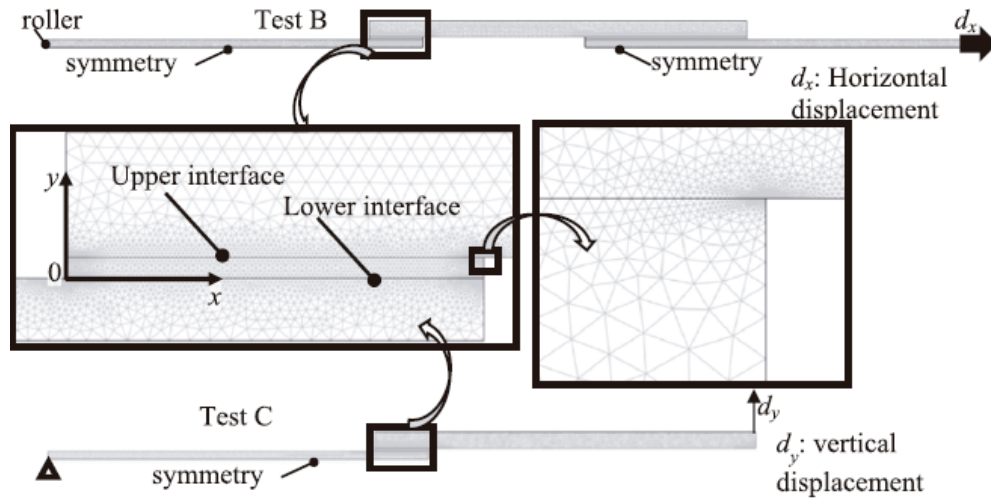
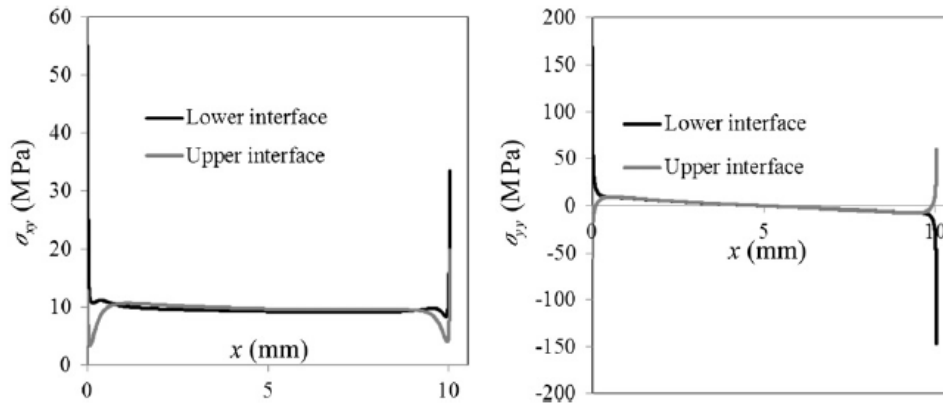Fig. 13. Meshing and boundary conditions (tests B and C).

Fig. 14. Interfacial normal and shear stresses (test B, $l=10$ mm).
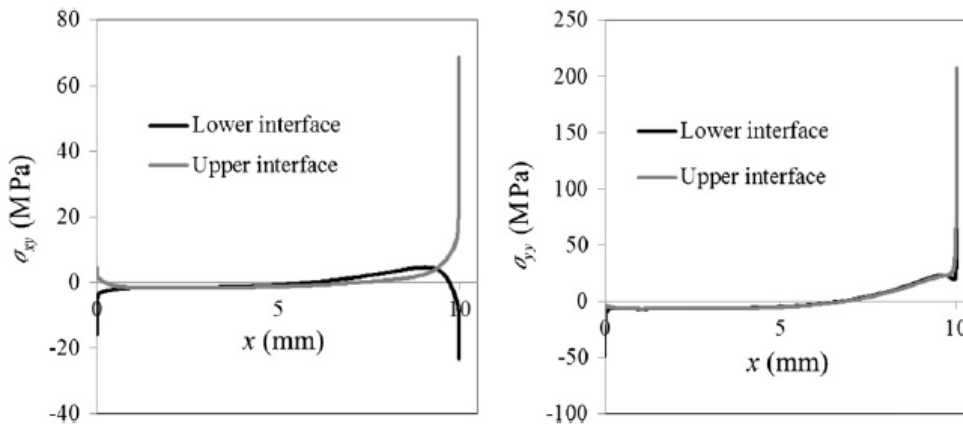

Fig. 15. Interfacial normal and shear stresses (test C, $l=10$ mm).

crack and subjected to a mechanical load. The equilibrium state is characterized by a potential energy Wp(0) and a zero kinetic energy Wk¼0. Next, the same structure is considered after the onset of a crack of surface area A which may be non-infinitesimal. The energy balance between these states yields

$$\Delta W_p + \Delta W_k + G_c A = 0$$

Where ΔW_p and ΔW_k are the changes respectively in potential and kinetic energy (these changes may be non-infinitesimal), G_c is the fracture energy per unit surface (a material property). Since $\Delta W_k \geq 0$, Eq. (3) yields then a necessary condition for fracture [22]

$$-\frac{\Delta W_p}{A} \geq G_c$$

In this manner, for those cases when a non-infinitesimal interfacial crack appears unstably (as in tests A, B and C) the following energy condition must be met

$$G^{inc} = -\frac{W_p(A) - W_p(0)}{A} \geq G^c$$

Where A is the area of the crack, Wp(A) is the potential energy in the cracked structure, Ginc is the incremental strain energy release rate and Gc is the critical strain energy release rate: a property of the interface related to its toughness. In [22], Leguillon proves then that a sole criterion (an energy criterion or a maximum stress criterion) do not suffice to predict failure onset in any geometry or loading condition. The author proves that in order to create a crack of area A, the following conditions must be met simultaneously

- the incremental strain energy condition in Eq. (5),

- the stress criterion $f(\tau, \sigma) \geq 0$ at every point where the crack appears;

Where τ and σ are the interfacial shear and normal stresses, respectively.

Martin et al. [23] show that the use of the previous twofold criterion predicts accurately thickness and stacking sequence effects on delamination initiation in cross-ply composite laminates.

In this paper, a spontaneous crack connected to a stress singularity point causes failure onset. In order to predict the nucleation of a spontaneous crack of surface *A*, Leguillon's approach [22] is adopted and the following twofold criterion is considered

$$\begin{cases} G^{inc}(A) \geq G^c \\ \tau^2 + a\sigma \geq \tau_c^2 \end{cases} \text{ at every point of surface } A \text{ just before failure onset}$$

where *a* and τ_c are material parameters which represent the sensitivity of the interfacial strength to peel stresses and the shear strength, respectively. The parameters G^c, *a* and τ_c will be determined in Section 5.3
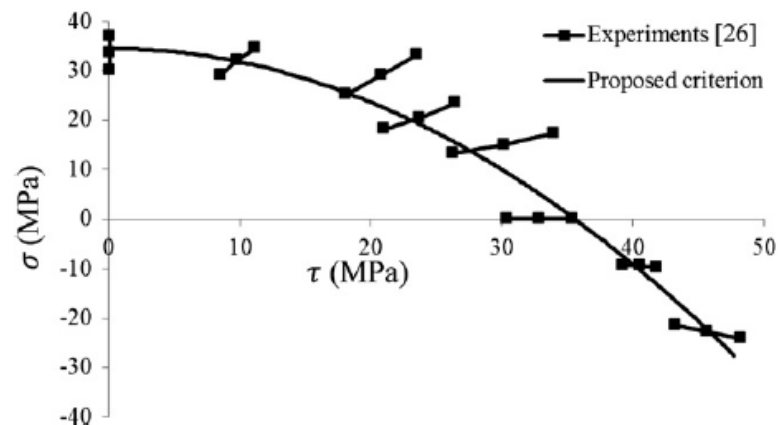

Fig. 16. Failure envelope of the adhesive joints tested in [26].

by fitting the theoretical predictions to the experimental results obtained in Section 2 of this paper. The stress condition adopted τ2+aσ≥τc2 is inspired by the shape of the experimental failure envelope in the τ−σ plane (τ and σ are the interfacial shear and normal stresses, respectively) shown in Fig. 16 and obtained by

Cognard et al. [26] with other materials (aluminum substrates bonded with an epoxy adhesive: Vantico Redux 420). Cognard et al. made a modification of the classical Arcan test in order to vanish the edge effects and to cause failure at the center of adhesive joints; the joints were tested in several load directions and both adhesive and cohesive failures were observed. Let us point out that the strength predicted by the proposed stress condition is sensitive to the sign of the peel stress, the same as the experiments performed by Cognard et al. [26].

5.2. Method to predict failure onset

The method to predict failure initiation is described by analyzing the example of type A specimens; for type B and C specimens, an analog method is applied. The following parameters are chosen arbitrarily to carry out the example of failure prediction: τ^c=10.0 MPa, a=10 MPa and G^c=70 J/m^2. In order to ease failure prediction, a monotonically increasing proportional loading is considered. The torque T and the axial tension force F are thus defined by

$$F = Q\cos(\alpha)\overline{F} \text{ and } T = Q\sin(\alpha)\overline{T}$$

Where α is a constant defining the loading direction, Q is an adimensional loading parameter, $\overline{F}$ =1kN and $\overline{T}$ =1Nm. Two loading cases are considered in this example of failure prediction

- pure tension (α=0°); this is the case of tests A1 in Table 2;
- torsion combined with tension verifying a 4 Nm/kN torque to force ratio (α=76°); this ratio is similar to that in tests A2 in Table 2.
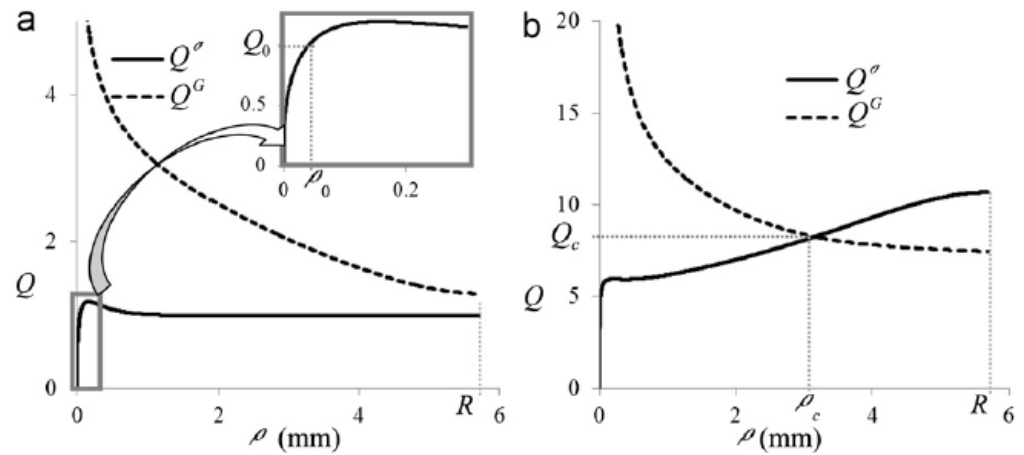
Fig. 17. Critical load parameters vs. crack depth or distance to the edge for the pure tension (a) and the torsion–tension (b) cases.
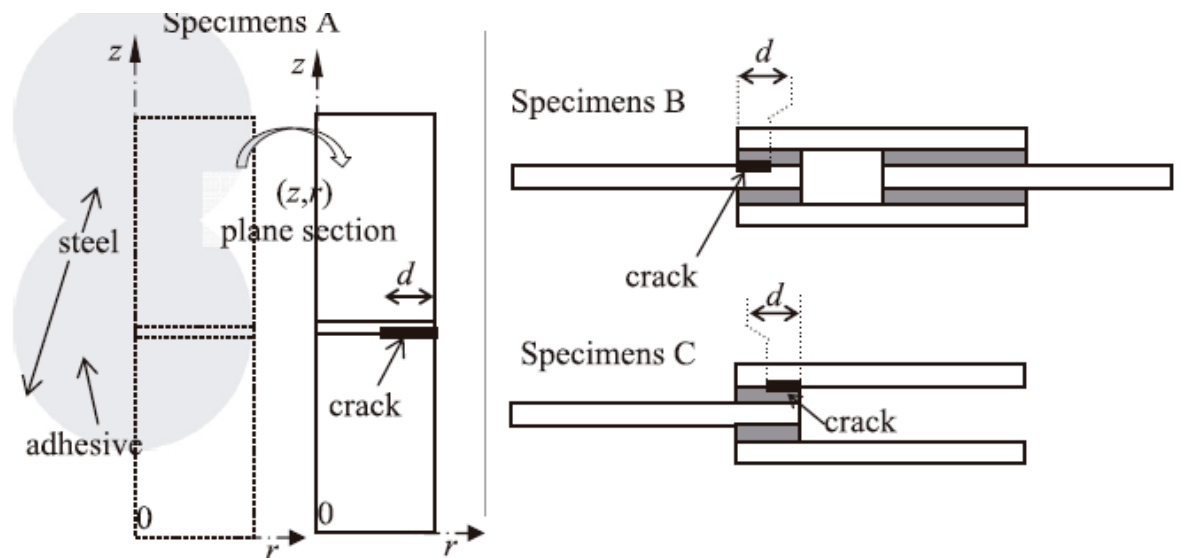

Fig. 18. Configuration of cracks considered to compute G^{Inc}.

The prediction of failure onset requires the calculation of interfacial stresses in uncracked specimens. By means of the results of the finite element software COMSOL it is possible to determine the interfacial stresses for each value of the radial position r. For tests A, the distance to the free edge is thus defined by $\rho=R-r$ (R is the radius of the specimen). Let us define the critical load Q^{σ} as the minimum positive load required to verify the stress condition in Eq. (6)

$$\sqrt{\sigma_{rz}^2(\rho)+\sigma_{\theta z}^2(\rho)+a\sigma_{zz}(\rho)}=\tau^c$$

In Fig. 17, the critical load Qs is plotted versus the distance r to the edge for the pure tension (a¼01) and the torsion-tension (a¼761) cases. It is worth mentioning that Qs tends to zero when r tends to zero. If the model assumes that only the strength criterion governs failure, it would predict meaninglessly that any load would cause failure initiation.

The prediction of failure onset requires also the computation of strain energies in cracked specimens so as to determine the incremental strain energy release rate Ginc in Eqs. (5) and (6).Itis worth mentioning that in this paper only one interfacial crack is modeled for each specimen instead of two symmetrical cracks because failure onset cracks appear spontaneously and failure initiates at the weakest interface or at the interface with greater defects. The location of the crack at one of the two possible interfaces was selected arbitrarily as shown in Fig. 18. At the end of Section 5.3, the theoretical results that would be obtained with two symmetrical cracks are commented. The surface area of the crack in all specimens is determined by the crack depth. For a type A specimen, a circumferential crack with a depth d in the
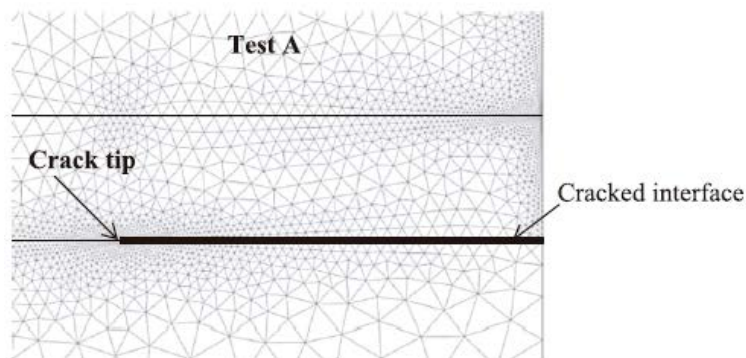

Fig. 19. Mesh for a cracked type A specimen.

radial direction is considered (see Fig. 18). For the other types of specimens, rectangular cracks with a depth d measured from the specimens edge are considered as shown in Fig. 18. In Fig. 19, the example of the meshing of a cracked type A specimen is shown. Owing to COMSOL calculations, for a given loading parameter Q_1, the incremental strain energy release rate G1inc(ρ) related to an interfacial crack connecting the free edge of the specimen A and a point located at the radial position $r=R-\rho$ is calculated ($\rho=d$ and R is the radius of the specimen). The consideration of the proportional loading allows determining the critical load $Q^G(\rho)$ required to obtain $G^{inc}(\rho)=G^c$ as follows:

$$Q^G(\rho) = Q_1 \sqrt{\frac{G^c}{G_1^{inc}(\rho)}}$$

This critical load $Q^G(\rho)$ is the minimum load required to create a spontaneous interfacial crack of depth ρ from an energy point of view. In Fig. 17, the critical load $Q^G(\rho)$ is plotted versus the depth ρ for the pure tension and the torsion-tension cases. If only the energy criterion $G^{inc} \geq G^c$ governed failure initiation, the load that would provoke failure would be $Q^G(R)$ and the crack would separate the specimen into two pieces. Now, let us analyze failure initiation by making use of the stress and energy criteria simultaneously. Let us first consider the case of pure tension. In Fig. 17(a), we observe that the curves of QG QUOTE and Qσ do not intersect. For a small loading level Q0, a small ρ0deep crack (see Fig. 17a) may appear from a stress point of view but this crack would not release enough energy to verify the energy criterion since QG(ρ0)>Qσ(ρ0). If the load parameter Q increases and attains the lowest value of QG (i.e. QG(R), R=5.7 mm), the stress and energy conditions in Eq. (6) are met simultaneously and the crack appears spontaneously breaking in two

parts the specimen. In this example, the failure in a pure tension test is controlled by the energy condition. Now, let us consider the case of the combined torsion–tension load. In Fig. 17(b), we observe that the curves of QUOTE QG and Qσ intersect at ρ=ρc=3.15 mm and Q=Qc=8.26. By following a similar reasoning as that for the pure tension test, one concludes that when the load parameter Q attains Qc, the load is enough to create a ρc deep crack from stress and energy point of views. The value of the load parameter that would cause failure initiation is then Qc=8.26 (i.e. F=0.765 kN, T=3.10 Nm).

5.3. Determination of parameters and results of failure onset prediction

Parameters G^c, a and τ^c are determined by fitting the predictions to the experimental data of tests A and B and applying a least square method. In this method, a first provisional set of values (G1c,a1,т1c) for these parameters is arbitrarily selected. The predictions of failure loads for tests A and B are then carried out by following the method detailed in the previous subsection. The sum S of the squared errors of these predictions compared to the experimental loads is then calculated. The gradient of S with respect to the parameters is calculated as well. With this gradient, a better set of parameters (G2c,a2,т2c) may be proposed by following the opposite direction of the gradient. These operations are repeated until the gradient is zero. The obtained values for the parameters are τ^c=13.0 MPa, a=15.2 MPa and G^c=52 J/m^2.
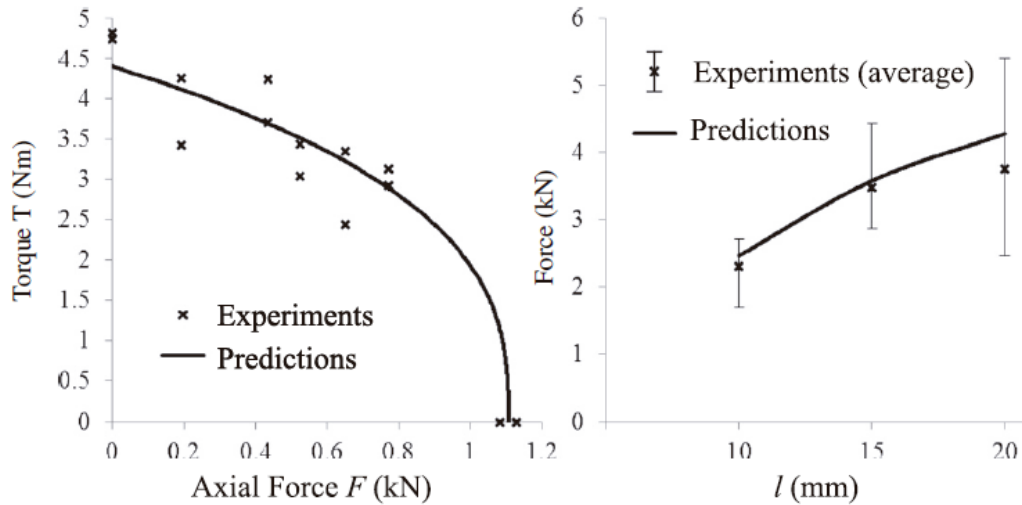
Fig. 20. Failure envelope for tests A (a) and failure load vs. overlap length l for tests B (b).

These parameters should be recalibrated if materials, substrate roughness and interface quality are changed. In Fig. 20, the curve fitting is shown for the failure envelope of specimens A and the graph of failure load against overlap length of specimens B. For specimens A, the criterion predicts correctly failure onset even for small positive axial forces. It seems that these predictions would have the same quality for negative axial forces. This will be confirmed in a subsequent study. For specimens B, the predictions lie within the range defined by the experimental data. Let us now apply the criterion to the prediction of failure onset in tests C. In Fig. 21, the experimental and theoretical forces that lead to failure of type C specimens are plotted against the overlap length l. Once again the predictions are accurate and lie within the range defined by the experimental data. Thus, the twofold criterion in Eq. (6) provides good quality predictions of failure and not only for tests A and B but also for tests C.

In Fig. 22, the predicted values of the crack depth at failure onset are plotted for tests A, B and C. Except for test A1, the crack depth lies between 0.8 mm and

2.7 mm. For test A1, failure is controlled by the energy condition in a similar manner as in the example of failure prediction in Section 5.2. After the crack appears, a thorough analysis (out of the scope of this paper) which takes into account the kinetic energy is required to determine the stability of the crack propagation. Finally, let us point out that the incremental strain energy release rates were also calculated in the case of two symmetrical
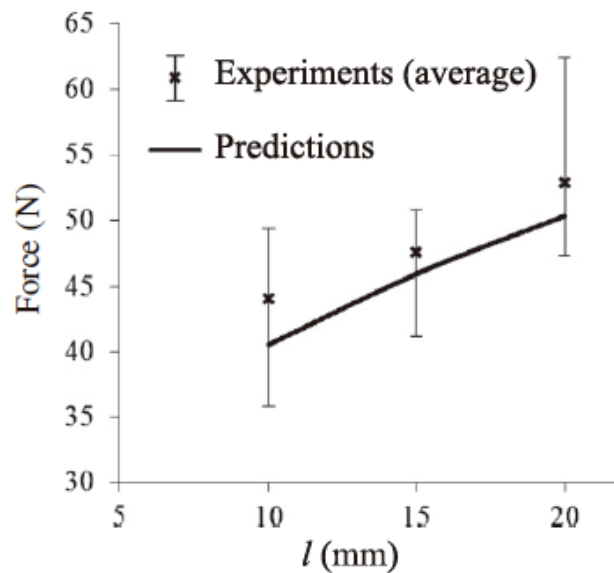

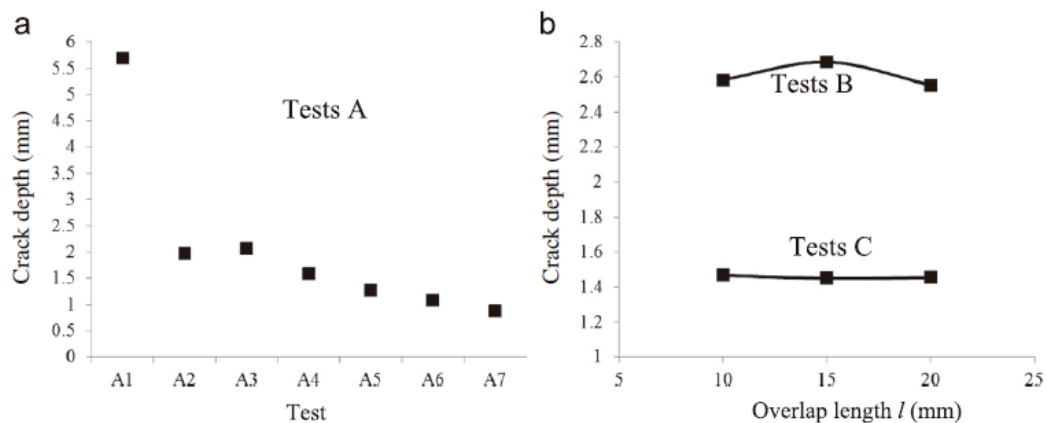Fig. 21. Experimental and theoretical failure loads vs. overlap length l (tests C).

Fig. 22. Theoretical crack depth at failure onset for tests A (a), B and C (b).
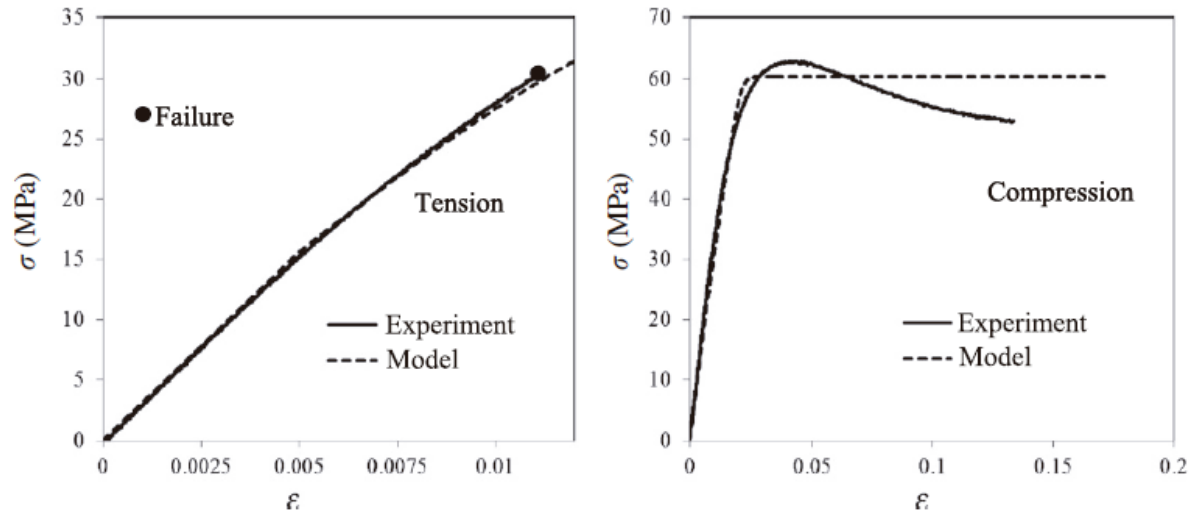
Fig. A.1. Fitting the stress–strain curves obtained in tension and compression.

Interfacial cracks and were compared to those in the case of one interfacial crack. For tests B and C, with the crack lengths shown in Fig. 22(b), the two cases (one crack, two cracks) provide practically the same results for the incremental strain energy release rate. For tests A, except for test A1, the two cases provided also the same results. For test A1, the incremental strain energy release rate in the case of one interfacial crack is greater than that of the case of two interfacial cracks. The correct failure scenario is the one that maximizes the incremental strain energy release rate: the case of one interfacial crack.

6. Conclusions

In this work, mechanical tests were performed to cause interfacial failures in adhesive joints specimens. These tests were carried out with double lap joints and butt joints submitted to combinations of axial load and torque. Failures were spontaneous and catastrophic. Before the failure, the adhesive used in all the specimens had plastic strains highly located around the stress singularity corners at the interfaces; this validated the use of a linear elastic model to calculate stresses in

the adhesive joints tested. A twofold criterion involving stress and energy conditions simultaneously was then applied to predict failure onset for the tested specimens by making use of finite element calculations. A stress condition, more appropriate than a quadratic stress criterion was applied. Good quality predictions were obtained.

The experimental results presented in this work may also help to test the validity of other adhesive failure criteria in predicting ailure for the different geometries and loading conditions assayed. A good criterion of interfacial failure depends only on the interface and not on the shape of the specimen. The twofold criterion applied in this paper and the proposed methodology to predict adhesive failure onset may be applied to predict failure onset in other adhesively bonded structures. For these reasons, this work is a good contribution to the prediction of the initiation of adhesive failure and particularly of the unstable crack nucleation at interfaces in adhesive joints.

It is worth mentioning that the method proposed herein to predict failure may be applied when nonlinearities are negligible. When nonlinearities such as plasticity in the adhesive are important, the energy balance leading to the energy condition involved in the twofold criterion must be revisited in order to take into account other dissipative phenomena. This will be performed in a subsequent paper.

Acknowledgments

Appendix A

In order to validate linear elastic calculations of interfacial stresses in the tested adhesive joints at failure onset, the results were compared to those obtained with non-linear calculations including an elastoplastic model for the adhesive. A Drucker–Prager type model with isotropic hardening was applied because the adhesive behavior is sensitive to the hydrostatic stress (see Fig. 4). In this model, the yield function is

$$f(\boldsymbol{\sigma}) = \sigma^{eq} + 3\mu\sigma^h - \sigma^0 - R(p)$$

where $\boldsymbol{\sigma}$, σ^{eq}, σ^h, μ, σ^0, p and $R(p)$ are the stress tensor, the Von-Mises stress, the hydrostatic stress, a material property, the initial yield stress, the cumulative plastic strain and the hardening function, respectively. An associated plasticity hypothesis and a normal flow rule were adopted. A hardening function with saturation was considered

$$R(p) = R_\infty (1 - e^{-\gamma p})$$

where R_∞ and γ are material properties. After fitting the experimental curves obtained in tension and compression for the bulk adhesive (see Fig. A.1), one obtains the material constants appearing in the model: μ=0.22, σ^0=19 MPa, R_∞=28 MPa and γ=700. Let us point out that this model does not predict failure of the adhesive material.

References

[1]   Grant LDR, Adams RD, da Silva LFM. Experimental and numerical analysis of single-lap joints for the automotive industry. Int J Adhes Adhes 2009;29: 405–13.

[2]   Park JH, Choi JH, Kweon JH. Evaluating the strengths of thick aluminum-to-aluminum joints with different adhesive lengths and thicknesses. Comp Struct 2010;92:2226–35.

[3]   Castagnetti D, Dragoni E, Spaggiari A. Failure analysis of bonded T-peel joints: efficient modeling by standard finite elements with experimental validation. Int J Adhes Adhes 2010;30:306–12.

[4]   Chataigner S, Caron JF, Duong VA, Diaz Diaz A. Experimental and numerical investigation of shear strain along an elasto-plastic bonded lap joint. Constr Build Mater 2011;25(2):432–41.

[5]   Keller T, Valle´ e T. Adhesively bonded lap joints from pultruded GFRP profiles. Part I: stress–strain analysis and failure modes. Compos Part B: Eng 2005;36:331–40.

[6]   Liljedahl CDM, Crocombe AD, Wahab MA, Ashcroft IA. Modeling the environ-mental degradation of adhesively bonded aluminum and composite joints using a CZM approach. Int J Adhes Adhes 2007;27:505–18.

[7]   Cognard JY, Cre´ ac'hcadec R, Sohier L, Leguillon D. Influence of adhesive thickness on the behaviour of bonded assemblies under shear loadings using a modified TAST fixture. Int J Adhes Adhes 2010;30:257–66.

[8]   Chataigner S, Caron J-F, Diaz Diaz A, Aubagnac C, Benzarti K. Non-linear failure criteria for a double lap bonded joint. Int J Adhes Adhes 2010;30: 10–20.

[9]   McCarthy J. Industry briefing: failure criteria for adhesive joints. AEA Technology (Harwell) Report; 1999.

[10]   Crocombe AD, Richardson G, Smith. PA. A unified approach for predicting the strength of cracked and non-cracked adhesive joints. J Adhes 1995;49: 211–44.

[11]   Qian Z, Akisanya AR. An experimental investigation of failure initiation in bonded joints. Acta Mater 1998;46:4895–904.

[12]   Kim KS, Yi YM, Cho GR, Kim CG. Failure prediction and strength improvement of uni-directional composite single lap bonded joints. Compos Struct 2008;82:513–20.

[13]   Brewer JC, Lagace PA. Quadratic stress criterion for initiation of delamination. J Comp Mater 1988;22:1141–55.

[14]   Mendoza-Navarro LE, Diaz-Diaz A, Caron JF, Chataigner S. Enhanced layer-wise model for laminates with imperfect interfaces. Part 2: Experimental validation and failure prediction. Compos Struct 2012;94:1032–7.

[15]   Sugiman S, Crocombe AD, Aschroft IA. Modelling the static response of unaged adhesively bonded structures. Eng Fract Mech 2013;98:296–314.

[16]   Khoramishad H, Crocombe AD, Katnam KB, Ashcroft IA. Predicting fatigue damage in adhesively bonded joints using a cohesive zone model. Int J Fatigue 2010;32:1146–58.

[17]   Katnam KB, Sargent JP, Crocombe AD, Khoramishad H, Ashcroft IA. Char-acterisation of moisture-dependent cohesive zone properties for adhesively bonded joints. Eng Fract Mech 2010;77:3105–19.

[18]   Liljedahl CDM, Crocombe AD, Wahab MA, Ashcroft IA. Modeling the environ-mental degradation of adhesively bonded aluminum and composite joints

using a CZM approach. Int J Adhes Adhes 2007;27:505–18.

[19]   Sugiman S, Crocombe. AD. The static and fatigue response of metal laminate and hybrid fibre-metal laminate doublers joints under tension loading. Compos Struct 2012;94:2937–51.

[20]   Ikegami K, Fujii T, Kawagoe H, Kyogoku H, Motoie K, Nohno K, et al. Benchmark tests on adhesive strengths in butt, single and double lap joints and double-cantilever beams. Int J Adhes Adhes 1996;16:219–26.

[21]   Guan ZD, Wu AG, Wang J. Study on ASTM shear-loaded adhesive lap joints. Chin J Aeronaut 2004;17:79–86.

[22]   Leguillon D. Strength or toughness? A criterion for crack onset at a notch Eur J Mech A/Solid 2002;21:61–72.

[23]   Martin E, Leguillon D, Carrere. N. A twofold strength and toughness criterion for the onset of free-edge shear delamination in angle-ply laminates. Int J Solids Struct 2010;47:1297–305.

[24]   Wang CH, Chalkley P. Plastic yielding of a film adhesive under multiaxial stresses. Int J Adhes Adhes 2000;20:155–64.

[25]   Adams RD, Coppendale J, Peppiatt NA. Stress analysis of axisymmetric butt joints loaded in torsion and tension. J Strain Anal 1978;13:1–10.

[26]   Cognard JY, Davies P, Gineste B, Sohier L. Development of an improved adhesive test method for composite assembly design. Compos S